Title

From Nano to Micro: Evolution of Magnetic Domain Structures in Multidomain Magnetite

Journal

Geochemistry, Geophysics, Geosystems, 20(6)

ISSN

1525-2027

Authors

Nagy, Lesleis
Williams, Wyn
Tauxe, Lisa
et al.

Publication Date

2019-06-01

DOI

10.1029/2019gc008319

Peer reviewed

Geochemistry, Geophysics, Geosystems

RESEARCH ARTICLE
10.1029/2019GC008319

From Nano to Micro: Evolution of Magnetic Domain Structures in Multidomain Magnetite

Lesleis Nagy[1], Wyn Williams[2], Lisa Tauxe[1], and Adrian R. Muxworthy[3]

[1]Scripps Institution of Oceanography, La Jolla, CA, USA, [2]School of Geosciences, University of Edinburgh, Edinburgh, UK, [3]Department of Earth Science and Engineering, Imperial College London, London, UK

Key Points:
- Single-vortex domain states extend to at least 1,000 nm for cuboctahedral and spherical magnetite grains
- Single-vortex to multidomain transition seen as vortex core elongation along hard crystalline axes
- Models show domain wall widths of about 100 nm, close to that predicted for 71 degrees Bloch-like walls

Supporting Information:
- Supporting Information S1
- Movie S1
- Movie S2
- Figure S1
- Figure S2

Correspondence to:
L. Nagy,
l1nagy@ucsd.edu

Citation:
Nagy, L., Williams, W., Tauxe, L., & Muxworthy, A. (2019). From nano to micro: Evolution of magnetic domain structures in multidomain magnetite. *Geochemistry, Geophysics, Geosystems*, *20*, 2907–2918. https://doi.org/10.1029/2019GC008319

Received 7 MAR 2019
Accepted 15 MAY 2019
Accepted article online 20 MAY 2019
Published online 22 JUN 2019

Abstract Reliability of magnetic recordings of the ancient magnetic field is strongly dependent on the magnetic mineralogy of natural samples. Theoretical estimates of long-term stability of remanence were restricted to single-domain (SD) states, but micromagnetic models have recently demonstrated that the so-called single-vortex (SV) domain structure can have even higher stability that SD grains. In larger grains ($\gtrsim$10 μm in magnetite) the multidomain (MD) state dominates, so that large uniform magnetic domains are separated by narrow domain walls. In this paper we use a parallelized micromagnetic finite element model to provide resolutions of many millions of elements allowing us, for the first time, to examine the evolution of magnetic structure from a uniform state, through the SV state up to the development of the domain walls indicative of MD states. For a cuboctahedral grain of magnetite, we identify clear domain walls in grains as small as $\sim$ 3 μm with domain wall widths equal to that expected in large MD grains; we therefore put the SV to MD transition at $\sim$ 3 μm for magnetite and expect well-defined, and stable, SV structures to be present until at least $\sim$ 1 μm when reducing the grain size. Reducing the size further shows critical dependence on the history of domain structures, particularly with SV states that transition through a so-called "unstable zone" leading to the recently observed hard-aligned SV states that proceed to unwind to SD yet remain hard aligned.

1. Introduction

In paleomagnetism, we are primarily interested in the ability of naturally occurring magnetic minerals to retain reliable magnetic recordings of external fields over timescales up to the age of the solar system. For many years, our understanding of stable remanences has relied on analytic theories of Néel (1949, 1955) and Stoner and Wohlfarth (1948). These theories make the assumption that a particle's magnetization is perfectly uniform and predict that the magnetic stability of single-domain (SD) grains increases with grain size up to a maximum size d_0 called the critical singe-domain grain size. Together, the theories of Néel and Stoner-Wohlfarth have laid the foundation for much of the early theory relating to man-made recording technologies. Yet it has long been appreciated (Gottschalk, 1935; Nagata, 1953) that the characteristics of magnetic materials vary rapidly with grain size, in a manner not expected from prevailing theory.

In contrast to the well-defined particles used in the magnetic recording industry, rock samples used in paleomagnetic studies generally have complicated magnetic mineralogies and a wide grain size distributions that extends well above d_0 (Roberts et al., 2018). Experimental observations (Day et al., 1977; Gottschalk, 1935; Stacey, 1963; Stacey et al., 1961) have shown us that the stability of grains larger than the expected threshold size, decreases only gradually, rather than suddenly as might have been expected from traditional theories of multidomain (MD) behavior. Such grains, larger than d_0 but exhibiting better than expected magnetic recording properties similar to SD, were termed pseudo-single-domains (PSD) by Stacey (1961). The nature of PSD grains remained poorly understood until the advent of three-dimensional numerical micromagnetic modeling (Schabes & Bertram, 1988; Williams & Dunlop, 1989) that was able to determine the detailed structure of nonuniform domains and discovered the, by now familiar, flower and vortex states. These numerical predictions have subsequently been verified via improved nanometric imaging of magnetic structures (Dunin-Borkowski et al., 1998). More recently, Nagy et al. (2017, 2019) demonstrated that vortex states have magnetic recording fidelity and stability equal to, and even exceeding that, of SD grains, thereby theoretically extending the grain size range capable of holding a paleomagnetically meaningful signal by at least an order of magnitude. Roberts et al. (2018) recently suggested abandoning the term PSD in favor of

vortex behavior, as the former term implies an ambiguous domain structure with unknown or undefined mechanisms of magnetic recording, which no longer holds true.

With the exception of Nagy (2016) and Valdez-Grijalva et al. (2018) who looked at single-vortex (SV)-MD transition in magnetite and greigite, respectively, little attention has been given to the transition from the vortex state to the magnetically unstable MD states. The SV to MD transition is of particular interest because recent numerical models of thermal stability in small single-vortex (SV) grains (Nagy et al., 2017) have shown that grains containing an easy-aligned SV domain state behave similarly to SD grains, in that switching between stable states occurs by coherent rotation of the magnetic domain structure. This structure-coherent rotation requires substantial energy and so these domain states exhibit both the high blocking temperatures and the high temporal stability required for retaining recordings of magnetic fields over geological timescales.

In contrast to the stable SV state, "true" MD states change via domain wall motion. Unless pinned by a crystal defects, MD walls move easily in response to changing external fields and are poor paleomagnetic recorders. It is important to understand the nature of the transition from the stable SV states to the unstable MD states so as to better determine the grain size range capable of carrying reliable paleomagnetic recordings.

Observing magnetic behavior of such small particles experimentally is challenging. To observe the magnetization inside a particle requires that it be electron transparent, that is, ~200 nm or less. For larger particles, there are many techniques for observing surface magnetization structures, but they do not allow us to look at the magnetic structure inside the particle. Only numerical modeling can currently allow us to do this.

In this paper we explore the particular case of the evolving magnetic domain structure in spherical and cuboctahedra particles of magnetite. We observe the change in domain state from SD to SV and then the evolution of domain walls typical of what we expect in MD states as we increase the grain size. We then shrink the grain and examine the minimum grain sizes that hold MD and SV domain states. In order to achieve this, we use a parallelized finite-element micromagnetic model Nagy et al. (2019), capable of providing model resolutions of many millions of elements.

2. Materials and Methods

We use a standard micromagnetic approach in this study. Given a magnetic region Ω, we find the unit vector along the magnetization $\vec{M}$, here $\hat{\eta}$ (i.e., $\|\hat{\eta}\| = 1$), that minimizes the effective field energy. This energy has three possible sources: (1) E_a, the magnetocrystalline anisotropy interaction, (2) E_e, the exchange interaction, and (3) E_d, the energy resulting from the self demagnetizing field, $\vec{H}_d$. These three energy terms can be expressed as follows:

$$E_a = K_1 \int_\Omega (\eta_1^2\eta_2^2 + \eta_1^2\eta_3^2 + \eta_2^2\eta_3^2)\, dV, \tag{1}$$

$$E_e = \frac{A}{L^2} \int_\Omega (\Delta\hat{\eta})^2\, dV, \tag{2}$$

$$E_d = -\frac{\mu_o M_s}{2} \int_\Omega \vec{H}_d \cdot \hat{\eta}\, dV, \tag{3}$$

where K_1 is the dominant magnetocrystalline anisotropy term, A is the exchange constant, M_s is the saturation magnetization, and L is the length scale at which we choose to measure our particles (in this study we use 10^{-9} m, i.e., nanometers). The room temperature values for K_1, A, and M_s used to model magnetite in this study are listed in Table 1. Equations (1) and (2) are computationally cheap to calculate as they are highly local. Computation of equation (3) proceeds by solving Maxwell's equations in a current-free regime. In this case it is possible to write $\vec{H}_d = -\nabla\varphi$, where φ is the magnetic scalar potential calculated by solving

$$\Delta\varphi = \begin{cases} -M_s \nabla \cdot \hat{\eta} & \vec{x} \in \Omega \\ 0 & \vec{x} \in R^3 \quad \Omega. \end{cases} \tag{4}$$

with the condition $\varphi \to 0$ as $\|\vec{x}\| \to \infty$.

Table 1
Material Parameters for Magnetite at Room Temperature

Parameter	Value	Unit	Source
K_1	-1.24×10^4	J/m^3	Bickford (1950)
A	1.33×10^{-11}	J/m	Heider and Williams (1988)
M_s	4.8×10^5	A/m	Pauthenet and Bochirol (1951)

Calculation of φ is computationally expensive as it is a result of long-range interactions involving each moment within the magnetic region. Several strategies are available to calculate φ, the most popular being the boundary element method (Fredkin & Koehler, 1990; Lindholm, 1984; Ó Conbhuí et al., 2018). Unfortunately, it is well known that the boundary element method results in a dense matrix-vector system, which leads to two problems: (1) the computation grows as $\mathcal{O}\left(N^2\right)$, where N is the number of vertices at the surface of the magnetic region, and (2) the problem is not well suited for parallelization, because each row of the dense matrix must fully participate in the resulting matrix-vector computation. The approach taken in this study uses a spatial transform technique (Figure 1) where the space outside the magnetic region Ω_s is also included in the finite element mesh and is bounded by a spherical shell of radius R_1. This sphere is then enclosed in a second shell of radius R_∞ representing the boundary at infinity where the condition $\varphi = 0$ can be applied. The spatial transform,

$$\vec{x}' = \left(\frac{R_1}{\|\vec{x}\|} \sqrt{\frac{R_\infty - R_1}{R_\infty - \|\vec{x}\|}} \right) \vec{x}, \tag{5}$$

is then used to distort the finite element shape functions within the region Ω_∞ in order to account for the condition that the magnetic scalar potential is zero at infinity (Abert et al., 2013; Brunotte et al., 1992; Imhoff et al., 1990a, 1990b). The integral form that solves equation (4) can then be split into three parts:

$$\int_{\Omega_\infty} J^{-1} \nabla v(\vec{x}) \cdot J^{-1} \nabla \varphi(\vec{x}) \, |J| \; \mathrm{d}V = 0, \tag{6}$$

$$\int_{\Omega_s} \nabla v(\vec{x}) \cdot \nabla \varphi(\vec{x}) \, \mathrm{d}V = 0, \tag{7}$$

$$\int_{\Omega} \nabla v(\vec{x}) \cdot \nabla \varphi(\vec{x}) \, dV = \mu_0 M_s \int_{\Omega} \nabla \cdot \hat{\eta} \, \mathrm{d}V, \tag{8}$$

where $v\left(\vec{x}\right)$ is the finite element shape function, and J^{-1} and $|J|$ are the inverse Jacobian matrix and Jacobian of equation (5), respectively (see supporting information section S1). The solution of equations (6) to (8) was implemented in the FEniCS finite element environment (Alnæs et al., 2015; Logg et al., 2012). This method results in a fully sparse matrix-vector system that is amenable to execution in a parallel environment Nagy (2016).

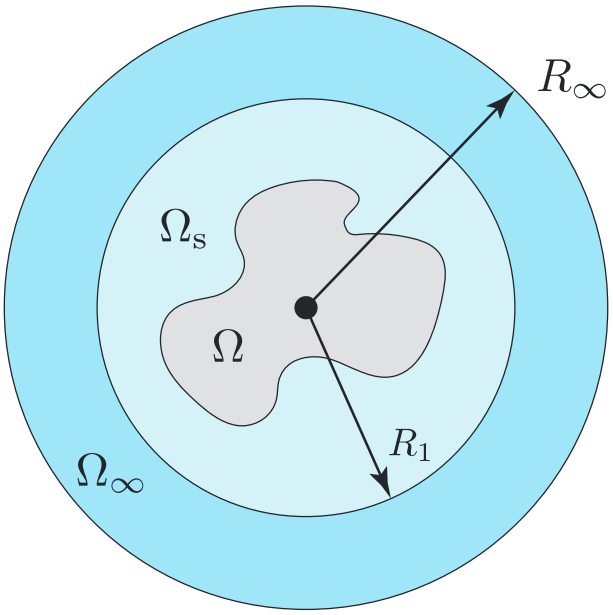

Figure 1. Schematic outlining the three regions of the method used. Ω is the magnetic region, which is enclosed in the free space region $\Omega_s \cup \Omega_\infty$. The region Ω_s corresponds to the area where no mapping is applied to solve for the magnetic scalar potential, whereas Ω_∞ corresponds to the region in which the mapping is applied.

2.1. Geometries, Meshing, and Processing

Two geometries were selected for this study, a sphere and cuboctahedron. The cuboctahedral geometry is shown in Figure 2 and was scaled using the scaling factor S in equation (9) to generate a cuboctahedron with volume equivalent to a sphere of diameter d:

$$S = \frac{1}{2}\left(\frac{\pi}{5}\right)^{\frac{1}{3}} d. \tag{9}$$

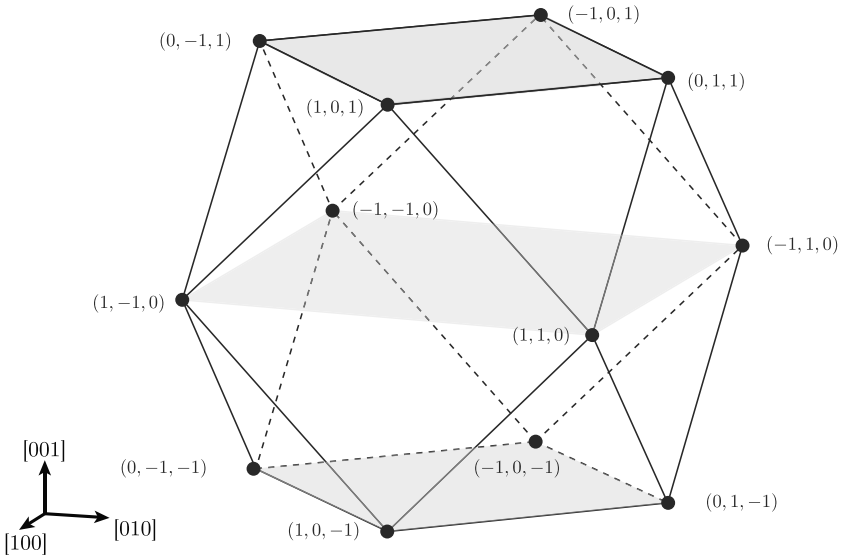

Figure 2. The cuboctahedral geometry used in this study. This geometry is uniformly scaled so that it occupies a volume equivalent to a sphere of a given diameter given by (9).

Meshes were generated using Trelis (Trelis, 2018) and element sizes between 7 nm (for smaller models) and 10 nm (for the largest models) were chosen as these values are both close to the 9-nm exchange length for magnetite (Rave et al., 1998). The exchange length is a guide to the maximum element size used in micromagnetic modeling so the values chosen here provide a good trade-off between accuracy and feasibility of performing computations (supporting information section S2).

Evolution of domain structures within the magnetite grain proceeded by first saturating the smallest model (30 nm), then minimizing for the total energy (equations (1)–(3)). This solution was then linearly interpolated to the next largest mesh and minimized again. The process continued until the model size reached 2,700-nm equivalent spherical volume diameter (ESVD) for cuboctahedra and 1,500-nm ESVD for spheres; the maximum sizes were selected given resource constraints. After reaching the maximum size, the geometry size was then reduced, repeating the minimizations between steps. Our micromagnetic models were run on the ARCHER supercomputer service (http://www.archer.ac.uk).

3. Results

3.1. Visualization

Results were visualized using Paraview (Ahrens et al., 2011; Ayachit, 2015). The image in Figures 3a and 3b illustrates a typical micromagnetic solution of a crystal in a single-vortex state. The difficulties in visualizing micromagnetic data with many vectors are apparent in the figure in that the high density of magnetic moments tends to obscure features of interest. We use two techniques in order to bring out structures in spin alignment. First, we color images by the anisotropic deviation of moment (ADM), denoted by Θ, which is a quantity derived from the directional component of the magnetocrystalline anisotropy energy:

$$\Theta = -\frac{1}{2}\left(1 - \left(\eta_1^4 + \eta_2^4 + \eta_3^4\right)\right), \tag{10}$$

with $-1/3 \leq \Theta \leq 0$, where $\Theta = 0$ corresponds to $\hat{\eta}$ aligned along a crystallographic hard axis (in magnetite) and $\Theta = -1/3$ corresponds to $\hat{\eta}$ aligned along a crystallographic easy axis. ADM is therefore the angle between a given magnetization vector and the nearest easy axis defined by the magnetocrystalline energy.

Additionally, we can summarize the magnetization structure using helicity, which is given by

$$H = \hat{\eta} \cdot (\nabla \times \hat{\eta}), \tag{11}$$

that is, the curl of the magnetization projected on to itself. Intuitively, high helicity corresponds to regions where the magnetization direction is changing rapidly, such as domain walls and regions surrounding the

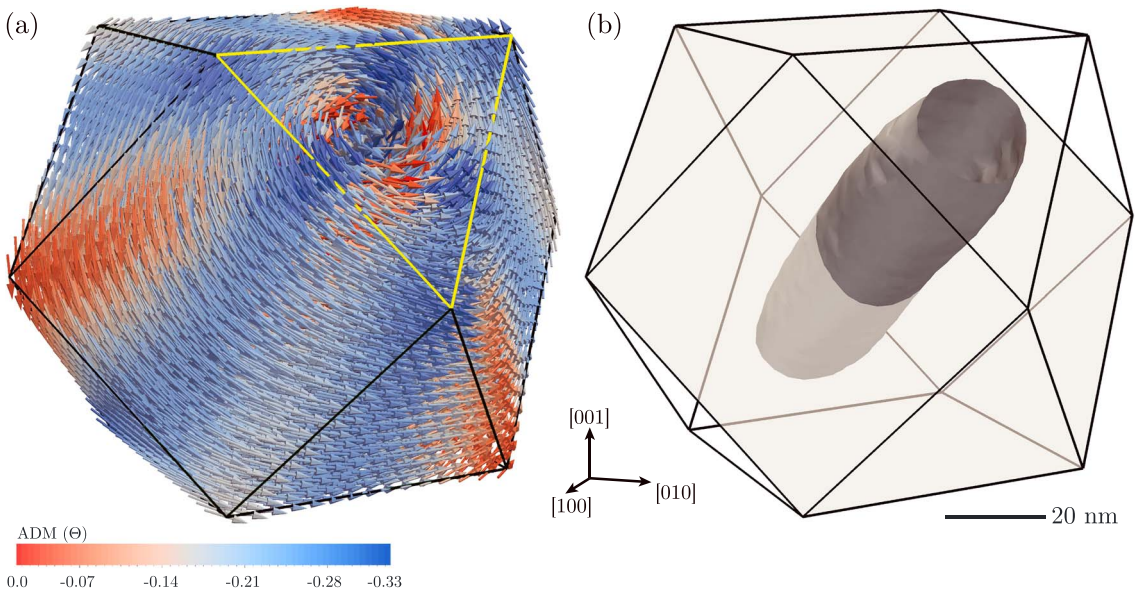

Figure 3. Vortex structure in a 100-nm cuboctahedron aligned along the [111] direction, (a) vectors have been colored by the anisotropic deviation of moment, ADM (10). A vortex core is visible on the [111] plane highlighted by the yellow triangle. (b) The helicity isosurface that corresponds to the vortex core.

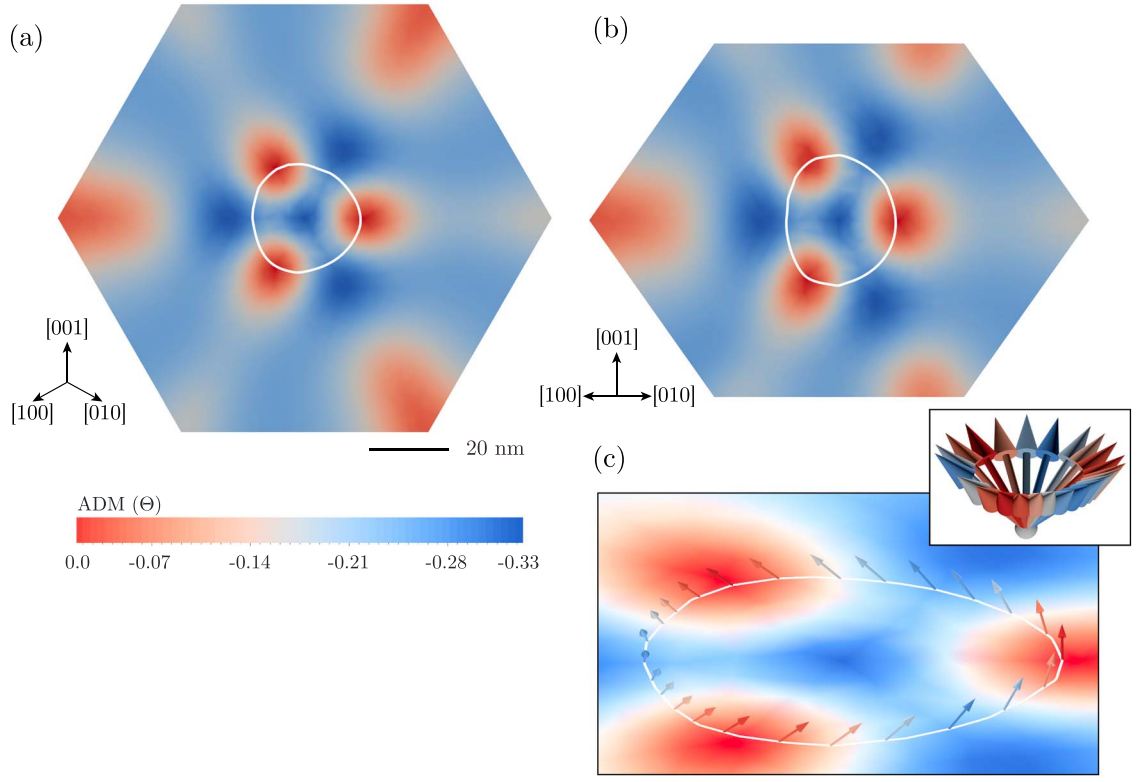

Figure 4. Anisotropy and helicity images for a 100-nm cuboctahedron. (a and b) Anisotropy slices in the (111) and (110) planes, respectively. The intersection between the anisotropy planes and the helicity surface from Figure 3b is shown as a white outline in (a) and (b). Dark red spots in (a) and (b) correspond to the helicity isosurface of the vortex core (Witt et al., 2005). (c) illustrates how the vectors along the isosurface line (the white line) rotate through a cone (inset) producing the high anisotropic deviation of moment (ADM) spots.

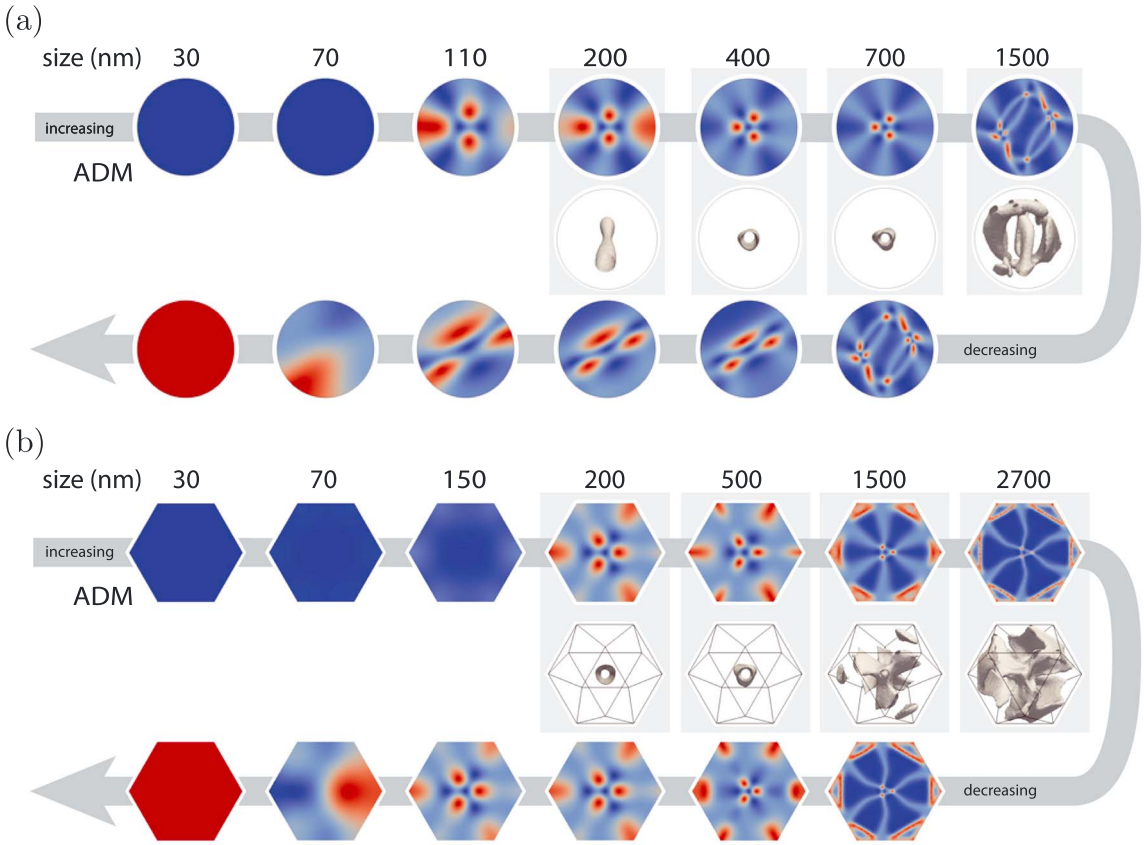

Figure 5. Subset of spherical and cuboctahedral models from the atlas shown in supporting information Figures S3 and S4. Helicity is shown in the (111) plane. The top row shows examples of solutions of anisotropic deviation of moment (ADM) starting with the 30-nm solution, which is then used to seed to subsequent sizes, etc. The middle row shows the helicity isosurfaces (associated with the increasing sequence), and the bottom row again shows the ADM solutions, beginning with the largest model from the top row as the starting point and decreasing grain size in increments back down to 30 nm. ADM color bar same as in Figure 4.

vortex cores. By selecting particular helicity values, it is possible to visualize an isosurface that highlights rapidly varying magnetization structures with the particle.

The images presented in Figure 4 highlight how ADM (equation (10)) and helicity (equation (11)) values are used throughout this study. Figures 4a and 4b show ADM values through the (111) and (110) planes respectively, whereas Figure 4c shows a cylindrical isosurface of constant helicity surrounding the vortex core. It should be noted how in ADM space the high helicity sheath around the vortex core is associated with three red dots in the anisotropy plane images (Figures 4a and 4b). These features occur because the vectors that correspond to the vortex core sheath trace out a cone with a base in the (111) plane (Figure 4c). Because this cone encompasses the three hard axes for magnetite, the magnetization vectors pass near to these hard axes resulting in three regions with vectors at high angles to the easy axes (high ADM), giving rise to the three red dots (see also Witt et al., 2005).

3.2. Effect of Increasing Grain Size

We consider the effect on domain state of growth of a crystal. In Figure 5 we show a subset of the results from the simulations for spherical grains for the purposes of discussion. The complete atlas of results for spherical and cuboctahedra is shown in Figure S3 and S4, respectively. In the case of both spherical and cuboctahedral models the initial state is a uniform magnetization in the [111] direction, illustrated by the uniform dark blue color in both spheres and cubes in Figure 5. As grain size increases, the domain state for cuboctahedra develops first into a flower state (as shown by faint lighter blue patches in Figures 5 and S4) for the 150-nm (ESVD) crystal. By 200 nm, the cuboctahedra has a well-defined SV state as illustrated by the characteristic three red dots in the ADM color maps and the helicity isosurface oriented in the [111] direction. Once the SV state is established in the cuboctahedra, the SV core is aligned along the [111] direction until at least

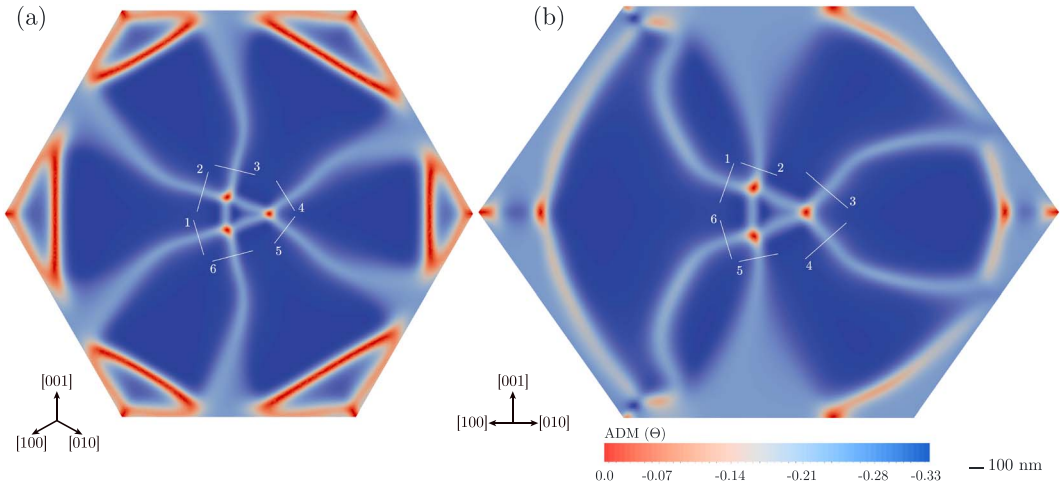

Figure 6. Anisotropy energy values for the the 2,700-nm equivalent spherical radius cuboctahedra in two planes. The model is believed to be entering the multidomain state and shows evidence of complex domain structure, with domains (in dark blue lying along the easy axes) separated by domain walls (lighter blue lines). The numbers in each figure denote the walls in (Table 3) and angle through which each domain rotate (Table 2) ADM = anisotropic deviation of moment.

400 nm. By 500 nm, however, the rounded, cylindrical shape of the helicity isosurface begins to resemble a structure reminiscent of a twisted-triangular prism (TTP).

There is no flower state for the spherical geometries. Instead, the ADM color map for the 110-nm spherical grain shows a sudden change in the domain structure to the single vortex (SV), highlighted by the three spots in Figure 5. But these spots are asymmetric about the [111] direction suggesting that the SV core is not aligned perfectly with the magnetocrystalline axis. This asymmetry persists until the 400-nm model. The transition can be seen most clearly by observing the [111] orientated helicity isosurfaces, which show the core sheath rotating from [110] to [111]. As in the cuboctahral case, the spherical helicity isosurfaces also show evidence of a TTP-like structure by 400 nm.

Examining the anisotropy energy surfaces for spheres in the 200- to 400-nm size range, the 200-nm sphere shows four red spots in the ADM maps, with the top and bottom most spots smeared, this is due to the fact that the [111] slice plane and the vortex core are not aligned. As the vortex core rotates to the [111] direction, the three red spots characteristic of a vortex core can be seen as expected. These spots appear to "tighten up," that is, become smaller and closer, as size increases and the helicity isosurface begins to resemble the TTP structure. The tightening up of the three red spots is also observed in the cuboctahedral grains, but to a lesser extent, and again corresponds to the vortex core transitioning from a cylinder to a TTP.

In spheres, the 500- to 1,200-nm size range shows little development with increasing grain size (Figure S3). Flattening of the side isosurface becomes more pronounced and the red spots in the ADM color maps continue to tighten. Between 400 and 700 nm, light blue spokes of higher-energy anisotropy regions can be observed eminating from the red spots outward toward the grain surface. These regions separate successively larger dark blue regions of low ADM. The clearest example is the 1,200-nm sphere (Figure S3), which hints toward a possible final domain structure with dark blue domains and lighter blue walls. The clear implication is that as the grain size increases, regions of uniform magnetization grow aligned with the easy magnetocrystalline axes and can be considered protodomains, while hard-aligned (e.g., [110]) regions between them are reduced. There is a rapid rotation of the magnetization that is the initial formation of domain walls.

In cuboctahedra, the size range 500 to 1,200 nm shows much more development in the domain structure compared to the spheres. At the ends of the isosurfaces, fins along the hard crystalline axis begin to emerge (700 nm), whereas the center of the isosurface continues to becomes more triangular (observe the center three spots tightening). By 1,200 nm, the fins are well developed and resemble a propeller structure, with the lobes oriented at 45° to each other; this is most clearly seen in column VII of Figure S4. Again, spokes can be observed emanating from the core spots to the grain edge in the 1,200-nm cuboctahedra, seen most

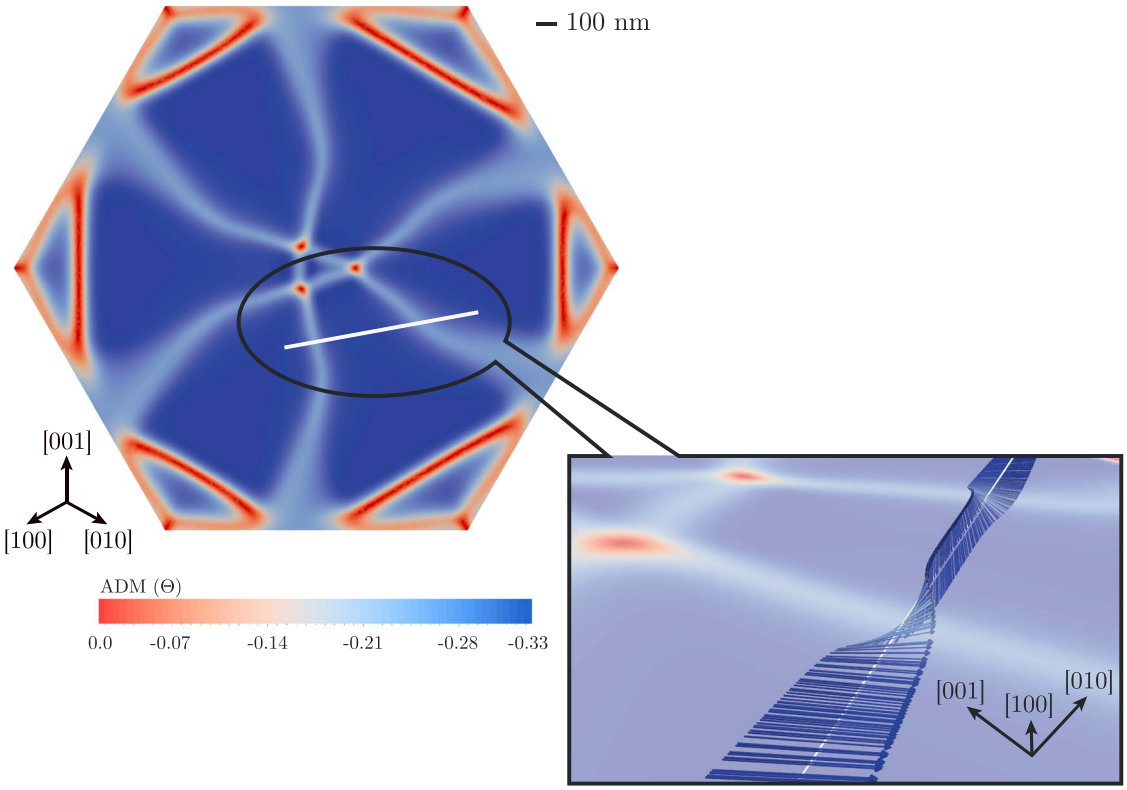

Figure 7. Bloch-like walls in the (111) plane. The white line on the right indicates the region in which the magnetization is evaluated. The inset image shows the magnetization along this line with respect to the plane, made transparent so that the rotation of vectors through the plane is apparent. It can be seen that there is significant rotation through the plane, along with some degree of rotation within the plane as the magnetization swings from one easy axis to another.

clearly in the ⟨1, 1, 1⟩ anisotropy slice. This is similar to what is observed for spheres, but the fanning out of the spokes representing the evolution of domain walls is greater in cuboctahedra, and the dark blue domains are smaller. Furthermore, the corners show small regions of high anisotropy that are likely a result of the grain geometry.

The transition from 1,200 to 1,500 nm is sudden in spheres. Both the ADM color maps and the helicity isosurfaces show evidence of a complex multivortex domain structure in the 1,500-nm model. The ADM images, in particular, show some evidence of dark blue domains with magnetization vectors oriented along easy axes, especially in the center, as well as possible closure domains developing near the surface.

For cuboctahedra, the transition to a MD state is more gradual and the domain structure hinted at in the 1,200-nm particle continues to develop and become more defined. This is particularly evident in the ADM images, where the gradual broadening out of the light blue spokes becomes tighter. Furthermore, the development of structures resembling closure domains becomes more distinct at the corners (columns I and III of Figure S4). It is likely that this domain structure will continue to become more and more refined as the size of the grain is increased. Unfortunately, due to the constraints of available computer resources and time, it was not possible to simulate larger grain sizes. However, the transition from SV to MD structure is clear by the 2,700-nm model (the largest grain that was simulated), and we examine this in section 3.4.

3.3. Effect of Decreasing Grain Size and the Hard-Aligned Single Vortex

The bottom row of Figure 5 shows the effect of decreasing grain size, summarizing the more complete results in Figures S3 and S4. As the grain size reduces, there is evidence that the complex structures found in larger grains persist to smaller grain sizes for both the sphere and the cuboctahedra. In spheres, for example, the complex structure observed at 1,500 nm persists until the size is reduced to 500 nm at which point there is once more a sudden transition to a single-vortex state, albeit a distorted one. The complex structure observed in the 2,700-nm cuboctahedron disappears more gradually until it becomes a vortex structure at 700 nm, although the fins at the tube ends when viewing the isosurfaces are still visible.

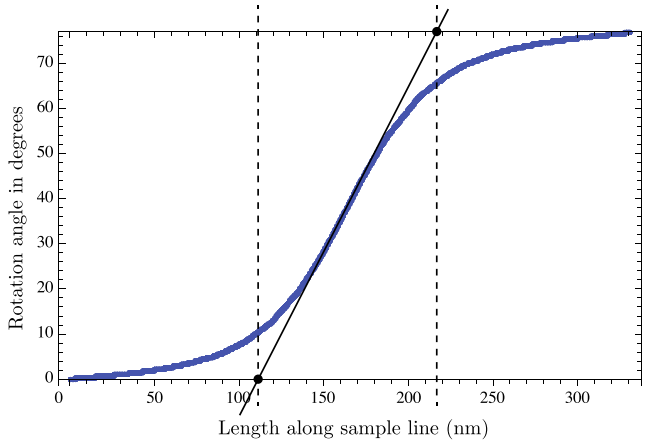

Figure 8. The graph shows the anisotropy energy plotted along the 1 and 6 sample lines of Figure 6. The linear part of the sigmoid of best fit is used to estimate the wall width indicated by the dotted vertical lines.

The vortex state finally collapses into a flower state by about 70 nm for both cuboctahedra and spheres, the final state for both being uniform structures along the hard directions (red) [001] for spheres and [00$\bar{1}$] for cuboctahedra.

The collapse of the vortex into a hard-aligned direction is an important result that we wish to highlight and is consistent with observations from numerical micromagnetic studies derived from completely random inital states (Nagy et al., 2019, 2017; Valdez-Grijalva et al., 2018). These studies found that grains within a so-called "unstable zone" (~85 to ~100 nm in magnetite) have domain structures predominantly aligned toward a hard axis. We see that as the size is decreased, the single-vortex domain structure must transition through the unstable zone where it becomes trapped as the core begins to unwind. The solution is caught in some weakly metastable state, and energy minimization is unable to overcome some, possibly very small, energy barriers. It is likely that thermal fluctuations would cause these states to be ephemeral.

3.4. The 2,700-nm Grain

The images shown in Figure 6 are large versions of the anisotropy energy slices for the 2,700-nm cuboctahedral grain shown in Figure 5. In order to examine these slices in more detail, we approximate the angles between adjacent domains and the widths of domain walls. The structures that appear to be closure domains in Figure 6 are not included as it is believed that those structures are not yet completely formed, as indicated by a light blue coloring in their centers.

In Figure 6 we highlight what we interpret to be domains, numbering the Bloch-like body domain walls that separate these domains (1–6). Figure 7 shows the magnetization along a line through a domain wall for the (111) plane; the magnetization rotates through an angle of 71.5° in the domain wall. It can be seen that there is significant amount of rotation through the plane as would be expected in a Bloch wall.

In order to estimate wall widths, locations were chosen which minimize possible wall distortion form the grain surface or vortex core. For the chosen locations (shown as white lines on Figure 6), the angle of rotation is taken along the line and results in the sigmoid graph as illustrated in Figure 8. The linear part of the graph corresponds to the region in which the magnetization vectors are rotating the most rapidly and therefore define the width of the domain wall. By fitting a line along the linear region of the sigmoid and projecting to the maximum/minimum angles, we can estimate the wall width to be at least 100 nm (Hubert & Schäfer, 1998; Lilley, 1950) in size.

It is expected that the magnetization within domains would be directed along one of the easy directions; therefore, the angles between domains should be one of 70.5°, 109.5°, or 180° as these are the only angles available between vectors directed along the diagonals of a cube. Table 2 shows the angles between the

Table 2
Estimated Domain Angles in the $\{1,1,0\}$ *and* $\{1,1,1\}$ *Planes Across Domain Walls Corresponding to the Lines in Figure 6*

Domains	$\langle 1,1,1 \rangle$		$\langle 1,1,0, \rangle$	
	Angle	Error (%)	Angle	Error (%)
1 and 2	69	1.6	67	5.1
2 and 3	70	1.3	72	2.2
3 and 4	69	2.6	68	4.1
4 and 5	69	1.6	67	5.1
5 and 6	69	1.5	72	2.3
1 and 6	69	1.4	67	4.4

Note. The domain walls are defined by the two domains which they connect. The error value is the relative error of the measured angle with respect to the expected angle of 70.5°.

Table 3
Estimated Domain Widths in the (110) *and* (111) *Planes Along the Lines Indicated in Figure 6*

Wall no.	⟨1, 1, 1⟩		⟨1, 1, 0, ⟩	
	Length (nm)	Error (%)	Length (nm)	Error (%)
1	129	21	122	26
2	128	22	122	26
3	126	23	87	47
4	131	20	159	3
5	134	19	131	20
6	115	30	103	38

Note. The error value is the relative error of the measured wall width with respect to an expected wall width of 164 nm.

domains indicated in Figures 6a and 6b. As can be seen from the Table 2, all domains observed are 70.5° walls. The errors in domain wall angle in both (110) and (111) planes are small in both cases.

Dunlop and Özdemir (1997) gave estimates for the expected width of the domain walls according to

$$\delta_w = \pi \sin\left(\frac{\phi}{2}\right)\left(\frac{A}{K}\right)^{\frac{1}{2}}, \tag{12}$$

where δ_w is the domain wall width, ϕ is the angle through which the magnetization of the domain wall rotates and $K\left(=1.64\times10^3\ \mathrm{J/m^3}\right)$ is an effective anisotropy constant determined as the anisotropy energy per unit volume across the domain wall (see equation 5.8, Dunlop & Özdemir, 1997). Using the data in Table 1, we get an estimate for the domain wall width of 164 nm for a wall rotating through 70.5°. In Table 3 we compare this value to domain wall widths estimated from the models (Figures 7 and 8). As can be seen there is some variance, which could be partly due to estimations of domain width being prone to small errors since identification of the linear region in Figure 8, was done manually. Another factor could be that the domain structure observed is not yet fully developed since further increases in size could result in thinner, more distinct domain walls. It should be noted that the model in Dunlop and Özdemir (1997) is only a one-dimensional model that assumes that the magnetization only rotates in a single plane with $\Theta \in [0, 180]$). The one-dimensional models also assume that the contribution from the magnetostatic interaction is negligible for the internal domain walls. Finally, the Dunlop and Özdemir (1997) estimate requires an assumption for the value of K, which may not be well constrained.

4. Discussion and Conclusions

Our methodology provides the optimal conditions for gradual evolution of domain states: The grain geometries have a high degree of symmetry, and there are no thermal fluctuations that would facilitate domain state switching across energy barriers. Domain structures are therefore free to evolve until the energy between domain states entirely disappears (within the numerical accuracy of the optimization). Despite this we see a rapid change of domain state from SV to SD at ~70 nm for decreasing grain sizes in both spherical and cubo-octahedral grain shapes, in agreement with previous micromagnetic studies on magnetite (Fabian et al., 1996; Muxworthy & Williams, 2006). This study also shows that, in the absence of thermal fluctuations the SD state can persist up to ~200 nm (cuboctahedra) and ~110 nm (spheres). Such large SD states are not seen, however, when the thermal energy of the grains is taken into account (Nagy et al., 2017). Irrespective of the exact size at which the SD to SV transition occurs, which will inevitably be dependent on the exact grain morphology, the transition occurs abruptly, or at least over a very narrow grain size range of ~10 nm.

This relatively abrupt change in domain state from SD to SV is again seen at the SV to MD boundary for spherical grains but more gradually for cuboctahedral grains. Evolution of the vortex core occurs as extensions along the hard magnetocrystalline axis as fins that develop into multicore structures. These appear to be primitive Bloch-like 71° domain walls that separate uniform regions of magnetization (domains) aligned with the easy axes. This sharp transition occurs in grains as small as 700 nm for deceasing grain sizes in spheres and somewhat more gradually from ~900 nm for cuboctahedra. For increasing grain sizes, the SV

state persists until ~1,500 nm for increasing grain sizes in both spheres and cuboctahedra. Again, as for the SD-SV transition, the SV-MD transition grain size will be modified by thermal fluctuations. The large CPU requirements of modeling grain of theses sizes, however, means that no study has yet examined the energy barrier that exists between SV and MD states in the same size grain. Nevertheless, in terms of stability of paleomagnetic signals, we can estimate that SV domain states in magnetite will exist from ~70 nm to at least ~1,000 nm, thus providing a greatly enhanced size range of domain stability over that provided by the SD domain states. The formation of partial or incomplete closure domain structures in the models for micron-sized particles, that is, 0.5–5 μm, may explain the complex surface domain structures observed in magnetite grains in this size range (Geiß et al., 1996; Halgedahl & Fuller, 1980; Muxworthy & Williams, 2006).

The results that have been presented above are an important addition to the understanding of how MD structures evolve. The picture that emerges is that complex domain structures develop from a combination of fins in the helicity sheath enclosing the vortex core along with boundary domains emerging from the surface. This is particularly striking when considering the cuboctahedral models. When comparing the largest grain size (the 2,700-nm cuboctahedron) against theoretical results, there is a good agreement of estimated domain wall thickness with what is predicted by theory. Large body domains aligned along the easy axes are clearly present and what appear to be the start of closure domains are also seen. Comparing the angles between adjacent domains gives good correspondence between what is expected and estimates of domain wall widths seem to be on the same order of magnitude as calculated in Dunlop and Özdemir (1997).

Acknowledgments
This work is funded from several sources: W. W. and A. M. are grateful to the Natural Environmental Research Council (NERC, grants NE/J020966/1 and NE/S001018/1), and W. W. also acknowledges NERC grant NE/S011978/1 and European Research Council (Grant EC320832). L. T. acknowledges support by the National Science Foundation under Grants EAR1827263 and EAR1547263. Micromagnetic model data found in this publication is available at https://doi.org/10.7488/ds/2549.

References

Abert, C., Exl, L., Selke, G., Drews, A., & Schrefl, T. (2013). Numerical methods for the stray-field calculation: A comparison of recently developed algorithms. *Journal of Magnetism and Magnetic Materials*, *326*, 176–185.

Ahrens, J., Geveci, B., Law, C., Hansen, C., & Johnson, C. (2011). Paraview: An end-user tool for large-data visualization. In C. Hansen & C. Johnson (Eds.), *The visualization handbook* (pp. 717–733). Oxford: Academic Press.

Alnæs, M. S., Blechta, J., Hake, J., Johansson, A., Kehlet, B., Logg, A., et al. (2015). The FEniCS project version 1.5. *Archive of Numerical Software*, *3*(100), 9–23.

Ayachit, U. (2015). *The paraview guide: A parallel visualization application*. Kitware, Inc.

Bickford, L. R. Jr. (1950). Ferromagnetic resonance absorption in magnetite single crystals. *Physical Review*, *78*(4), 449–457.

Brunotte, X., Meunier, G., & Imhoff, J. F. (1992). Finite-element modeling of unbounded problems using transformations—A rigorous, powerful and easy solution. *IEEE Transactions on Magnetics*, *28*(2), 1663–1666.

Day, R., Fuller, M. D., & Schmidt, V. A. (1977). Hysteresis properties of titanomagnetites: Grain size and composition dependence. *Physics of the Earth and Planetary Interiors*, *13*, 260–266.

Dunin-Borkowski, R. E., McCartney, M. R., & Smith, D. J. (1998). Off-axis electron holography of magnetic materials. *Record Research and Development Applied Physics*, *1*, 119–131.

Dunlop, D. J., & Özdemir, Ö. (1997). *Rock magnetism: Fundamentals and frontiers*. Cambridge: Cambridge university press.

Fabian, K., Kirchner, A., Williams, W., Heider, F., Leibl, T., & Hubert, A. (1996). Three-dimensional micromagnetic calculations for magnetite using FFT. *Geophysical Journal International*, *124*(1), 89–104.

Fredkin, D., & Koehler, T. (1990). Hybrid method for computing demagnetizing fields. *IEEE Transactions on Magnetics*, *26*(2), 415–417.

Geiß, C. E., Heider, F., & Soffel, H. C. (1996). Magnetic domain observations on magnetite and titanomaghemite grains (0.5-10 μm). *Geophysical Journal International*, *124*, 75–88.

Gottschalk, V. H. (1935). The coercive force of magnetite powders. *Physics*, *6*, 127–132.

Halgedahl, S., & Fuller, M. (1980). Magnetic domain observations of nucleation processes in fine particles of intermediate titanomagnetite. *Nature*, *288*, 70–72.

Heider, F., & Williams, W. (1988). Note on temperature-dependence of exchange constant in magnetite. *Geophysical Research Letters*, *15*(2), 184–187.

Hubert, A., & Schäfer, R. (1998). *Magnetic domains: The analysis of magnetic microstructures*. Berlin, Heidelberg: Springer Science & Business Media.

Imhoff, J. F., Meunier, G., Brunotte, X., & Sabonnadiere, J. C. (1990b). An original solution for unbounded electromagnetic 2D- and 3D-problems throughout the finite element method. *IEEE Transactions on Magnetics*, *26*(5), 1659–1661.

Imhoff, J. F., Meunier, G., & Sabonnadiere, J. C. (1990a). Finite-element modeling of open boundary-problems. *IEEE Transactions on Magnetics*, *26*(2), 588–591.

Lilley, B. (1950). Energies and widths of domain boundaries in ferromagnets. *Philosophical Magazine Journal Science*, *41*(319), 792–813.

Lindholm, D. (1984). Three-dimensional magnetostatic fields from point-matched integral equations with linearly varying scalar sources. *IEEE Transactions on Magnetics*, *20*(5), 2025–2032.

Logg, A., Mardal, K.-A., & Wells, G. (2012). *Automated solution of differential equations by the finite element method: The FEniCS book* (Vol. 84). Berlin, Heidelberg: Springer Science & Business Media.

Muxworthy, A. R., & Williams, W. (2006). Critical single-domain/multidomain grain sizes in noninteracting and interacting elongated magnetite particles: Implications for magnetosomes. *Journal of Geophysical Research*, *111*, B12S12. https://doi.org/10.1029/2006JB004588

Muxworthy, A. R., & Williams, W. (2006). Observations of viscous magnetization in multidomain magnetite. *Journal of Geophysical Research*, *111*, B01103. https://doi.org/10.1029/2005JB003902

Nagata, T. (1953). *Rock magnetism*. Tokyo: Maruzen.

Nagy, L. (2016). Parallelisation of micromagnetic simulations (PhD thesis). The University of Edinburgh.

Nagy, L., Williams, W., Muxworthy, A. R., Fabian, K., Almeida, T. P., Conbhuiu, P., & Shcherbakov, V. P. (2017). Stability of equidimensional pseudo-single domain magnetite over billion year timescales. *Proceedings of the National Academy of Sciences of the United States of America*, *114*, 10,356–10,360.

Nagy, L., Williams, W., Tauxe, L., Muxworthy, A. R., & Ferreira, I. (2019). Thermomagnetic recording fidelity of nanometer-sized iron and implications for planetary magnetism. *Proceedings of the National Academy of Sciences of the United States of America*, *116*, 1984–1991.

Nagy, L., Williams, W., & Valdez-Grijalva, M. (2019). Micromag: A micromagnetics code for high performance computing (Version 0.0.1). Zenodo.

Néel, L. (1949). Théeorie du trainage magnétique des ferromagneétiques en grains fines avec applications aux terres cuites. *Annales Geophysicae*, *5*, 99–136.

Néel, L. (1955). Some theoretical aspects of rock-magnetism. *Advances in Physics*, *4*, 191–243.

Ó Conbhuí, P., Williams, W., Fabian, K., Ridley, P., Nagy, L., & Muxworthy, A. R. (2018). Merrill: Micromagnetic earth related robust interpreted language laboratory. *Geochemistry, Geophysics, Geosystems*, *19*, 1080–1106. https://doi.org/10.1002/2017GC007279

Pauthenet, R., & Bochirol, L. (1951). Aimantation spontanée des ferrites. *Journal de Physique et Le Radium*, *12*(3), 249–251.

Rave, W., Fabian, K., & Hubert, A. (1998). Magnetic states of small cubic particles with uniaxial anisotropy. *Journal of Magnetism and Magnetic Materials*, *190*(3), 332–348.

Roberts, A. P., Tauxe, L., Heslop, D., Zhao, X., & Jiang, Z. (2018). A critical appraisal of the 'Day' diagram. *Journal of Geophysical Research: Solid Earth*, *123*, 2618–2644. https://doi.org/10.1002/2017JB015247

Schabes, M. E., & Bertram, H. N. (1988). Magnetization processes in ferromagnetic cubes. *Journal of Applied Physics*, *64*, 1347–1357.

Stacey, F. D. (1961). Theory of the magnetic properties of igneous rocks in alternating fields. *The Philosophical Magazine: A Journal of Theoretical Experimental and Applied Physics*, *6*(70), 1241–1260.

Stacey, F. D. (1963). The physical theory of rock magnetism. *Advances in Physics*, *12*, 45–133.

Stacey, F. D., Lovering, J. F., & Parry, L. G. (1961). Thermomagnetic properties, natural magnetic moments, and magnetic anisotropies of some chondritic meteorites. *Journal of Geophysical Research*, *66*, 1523–1534.

Stoner, C. E., & Wohlfarth, W. P. (1948). A mechanism of magnetic hysteresis in heterogeneous alloys. *Philosophical Transactions of the Royal Society of London. Series A*, *240*, 599–642.

Trelis (2018). (Version 16.4) [Computer software]. American Fork, UT: csimsoft. http://csimsoft.com

Valdez-Grijalva, M. A., Nagy, L., Muxworthy, A. R., Williams, W., & Fabian, K. (2018). The magnetic structure and palaeomagnetic recording fidelity of sub-micron greigite (Fe3S4). *Earth and Planetary Science Letters*, *483*, 76–89.

Williams, W., & Dunlop, D. J. (1989). Three-dimensional micromagnetic modelling of ferromagnetic domain structure. *Nature*, *337*, 634–637.

Witt, A., Fabian, K., & Bleil, U. (2005). Three-dimensional micromagnetic calculations for naturally shaped magnetite: octahedra and magnetosomes. *Earth and Planetary Science Letters*, *233*(3), 311–324.